Structure and properties of ordered Li$_2$IrO$_3$ and Li$_2$PtO$_3$

Matthew J. O'Malley [a,b,*], Henk Verweij [b], Patrick M. Woodward [a]

[a] *Department of Chemistry, The Ohio State University, 100 West 18th Avenue, Columbus, OH 43210-1185, USA*
[b] *Department of Materials Science and Engineering, The Ohio State University, 477 Watts Hall, 2041 College Road, Columbus, OH 43210-1124, USA*

A R T I C L E   I N F O

A B S T R A C T

The structures of Li$_2M$O$_3$ (M = Ir, Pt) can be derived from the well-known Li-ion battery cathode material, LiCoO$_2$, through ordering of Li$^+$ and M^{4+} ions in the layers that are exclusively occupied by cobalt in LiCoO$_2$. The additional cation ordering lowers the symmetry from rhombohedral (R-3m) to monoclinic ($C2/m$). Unlike Li$_2$RuO$_3$ no evidence is found for a further distortion of the structure driven by formation of metal–metal bonds. Thermal analysis studies coupled with both *ex-situ* and *in-situ* X-ray diffraction measurements show that these compounds are stable up to temperatures approaching 1375 K in O$_2$, N$_2$, and air, but decompose at much lower temperatures in forming gas (5% H$_2$:95% N$_2$) due to reduction of the transition metal to its elemental form. Li$_2$IrO$_3$ undergoes a slightly more complicated decomposition in reducing atmospheres, which appears to involve loss of oxygen prior to collapse of the layered Li$_2$IrO$_3$ structure. Electrical measurements, UV–visible reflectance spectroscopy and electronic band structure calculations show that Li$_2$IrO$_3$ is metallic, while Li$_2$PtO$_3$ is a semiconductor, with a band gap of 2.3 eV.

1. Introduction

Solid-state pH sensors are highly desirable due to their stability at high temperatures, high pressures, and potential use in non-aqueous environments. Transition metal oxides such as RuO$_2$, IrO$_2$, and PtO$_2$ have been investigated as solid-state pH sensing materials since the mid-1980s [1,2], with IrO$_2$ showing the most promise. The use of a lithium carbonate melt process to produce solid-state iridium oxide pH sensors has been shown to produce sensors that are more stable and reproducible than other techniques used to produce iridium oxide-based pH sensors [3].

Carbonate melt-based sensors are produced via oxidation of an iridium wire in molten lithium carbonate [3–5]. The phases responsible and the mechanism behind the pH sensitivity of these systems are not well understood, despite their current use in commercial applications. Thus, knowledge of the structure and properties of phases produced via reactions between lithium carbonate and both Ir and Pt, are vital to further improving these sensors.

The stable phases obtained using traditional solid-state reactions between Li$_2$CO$_3$ and the platinum group metals (M = Ru, Ir, Pt) include Li$_2$RuO$_3$ [6–8], Li$_2$IrO$_3$ [9], and Li$_2$PtO$_3$ [10]. Of these phases the ruthenate has been most extensively studied. There are

relatively few reports of other ternary oxide phases forming, only Li$_3$RuO$_4$ [11], Li$_8$IrO$_6$ [12], Li$_8$PtO$_6$ [12], and Li$_{0.64}$Pt$_3$O$_4$ [13] have been reported. The structure of Li$_2M$O$_3$ can be described as an ordered variant of the rock salt structure containing cation layers that alternate between pure lithium layers and mixed metal layers, LiM_2 (Fig. 1). These phases are structurally and compositionally related to LiCoO$_2$ currently used as the cathode in lithium ion batteries.

The relative simplicity of the Li$_2$O–IrO$_2$ phase diagram suggests that Li$_2$IrO$_3$ may play a key role in the production and/or operation of miniaturized pH sensors produced via the lithium carbonate melt oxidation of iridium wires. Despite the technological importance of this material a number of questions regarding its structure, chemical stability, and physical properties remain unanswered. To address this deficiency we report here a systematic study of the structural, thermal, optical, and electrical properties of highly ordered Li$_2$IrO$_3$ and Li$_2$PtO$_3$. These are compared and contrasted with Li$_2$RuO$_3$.

2. Experimental

Li$_2M$O$_3$ (M = Ru, Ir, Pt) were prepared using stoichiometric mixtures of Li$_2$CO$_3$ (J.T. Baker, 99.2%) and either Ru (∼325 mesh, Cerac, 99.95%), Ir (∼325 mesh, Alfa Aesar, 99.9%) or Pt (∼325 mesh, Alfa Aesar, 99.9+%). For all syntheses 5% excess Li$_2$CO$_3$ was added to compensate for high-temperature lithium volatility. The starting materials were mixed under isopropanol using an agate

---

* Corresponding author at: Department of Chemistry, The Ohio State University, 100 West 18th Avenue, Columbus, OH 43210-1185, USA.
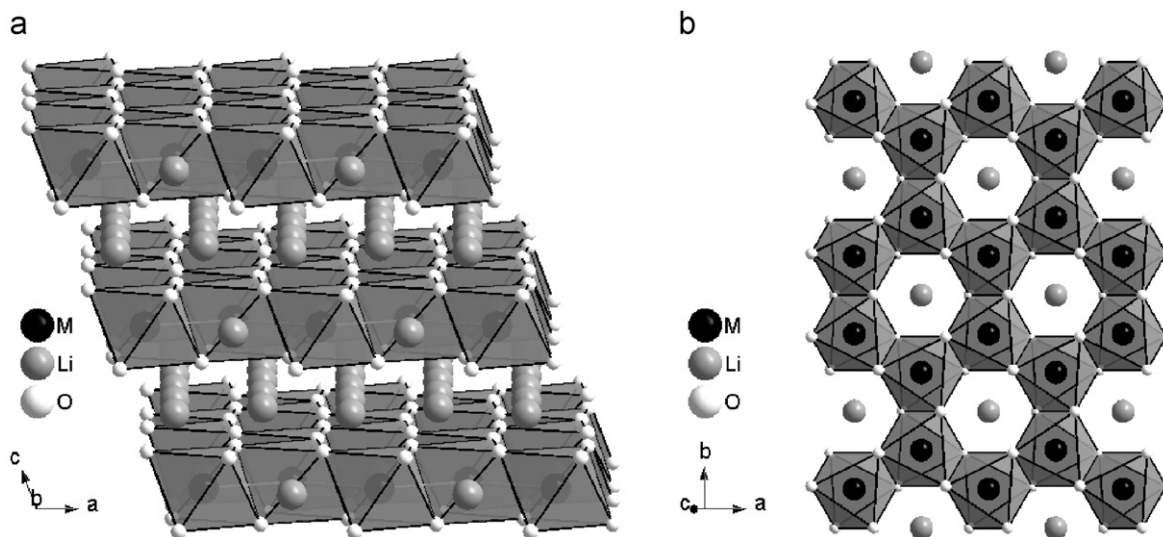*E-mail address:* momalley@chemistry.ohio-state.edu (M.J. O'Malley).

Fig. 1. The Li_2MO_3 structure shows the characteristic layering (a), as well as the LiM_2 layer with corresponding oxygens (b).

mortar and pestle, and placed in high-density alumina crucibles (Coorstek, 99.8%). The mixtures were then heated in air at a rate of 10 K/min to the initial target temperature of 1025 K and held at that temperature for 12 h before cooling back to room temperature at a rate of 10 K/min. Successive heating cycles were performed by increasing the annealing temperature in 50 K steps, up to 1325 K where pure ordered phases were obtained. Attempts to streamline the synthesis by pre-reacting the starting materials at 1025 K followed by heating directly to 1325 K lead to premature decomposition rather than the formation of highly ordered structures.

X-ray powder diffraction (XRPD) data were collected in Bragg–Brentano geometry using a Bruker D8 Advance X-ray powder diffractometer (40 kV, 50 mA, sealed Cu X-ray tube). This instrument is equipped with an incident beam Ge 1 1 1 monochromator, selecting only $CuK\alpha_1$ radiation ($\lambda = 1.5406$ Å), and a Braun linear position sensitive detector. The data were collected over the angular range $10° < 2\theta < 100°$ with a step size of $0.014265°$ and a counting time of 1 s per step. Structural refinements were completed using the Rietveld method as incorporated in the software package TOPAS Academic [14,15].

Thermo-gravimetric analyses (TGAs) were performed using a Perkin Elmer TGA 7 with TAC 7/DS Thermal Analysis Instrument Controller. Approximately 50 mg of sample was placed in a platinum boat for each analysis. The samples were heated to 1575 K with a heating rate of 10 K/min. A gas flow rate of 40 mL/min was used for reagent grade O_2, air, N_2, and forming gas (5:95, H_2:N_2).

High-temperature *in-situ* XRPD measurements in forming gas (5:95, H_2:N_2) were made using an Anton Paar HTK 1200 furnace in conjunction with the Bruker D8 Advance. The samples were heated to 673 K with a ramp rate set to 1 K/min and then held at constant temperature for each measurement. The *in-situ* XRPD data were collected over the angular range $17.5° < 2\theta < 47.5°$ with a step size of $0.072978°$ and a counting time of 0.5 s per step. The lattice parameters from the *in-situ* XRPD experiments were determined using Rietveld refinements. Due to the limited angular range over which the high-temperature data were collected the atomic parameters were constrained to be equal to their room temperature values.

UV–visible diffuse reflectance data were collected on polycrystalline samples using a Perkin-Elmer Lambda 20 scanning double-beam spectrometer equipped with a 50-mm Labsphere integrating sphere over the spectral range 400–1100 nm

(3.1–1.1 eV). The Kubelka–Munk function was used to convert the diffuse reflectance data into absorption data. The band gap energies reported were determined using Shapiro's method of extrapolating the onset of absorption to the wavelength axis [16].

Electronic structure calculations were performed using the Cambridge Serial Total Energy Package (CASTEP) [17]. CASTEP is a first principles density functional theory (DFT) plane wave pseudo-potential simulation code. The calculations were performed in the frame of the generalized gradient approximation (GGA) as derived by Perdew and Wang (PW-91) for the exchange and correlation effects [18,19]. A Gaussian smearing scheme of 0.05 eV was employed when drawing the density of states (DOS) plots.

Alternating current (AC) electrical measurements were performed using a Solartron SI 1260 Impedance/Gain-Phase Analyzer scanning from 10^7 and 1 Hz, over the temperature range 300–800 K. Compact pellet samples were prepared using uniaxial pressing (230 MPa) followed by heating at 1300–1400 K for 4 h. The circular pellets were sanded to obtain a smooth surface before making electrical contacts with silver paint, (Ted Pella, Leitsilber 200) connected via gold mesh contacts. The material that was removed from the pellet during sanding was analyzed using XRPD on a zero-background sample holder to verify that sintering did not alter the phase purity.

3. Results and discussion

3.1. Structural characterization

There is some debate in the literature regarding the proper choice of unit cell and space group symmetry of the Li_2MO_3 phases. Li_2IrO_3 has been reported using $C2/c$ ($Z = 8$) symmetry [9], as has Li_2RuO_3 [6–8], while Li_2PtO_3 has been reported to possess $P3_1$ ($Z = 6$) [20] and $C2/m$ ($Z = 4$) symmetry [21]. A recent neutron diffraction study on Li_2RuO_3 reported $C2/m$ symmetry ($Z = 4$) at 600 K [22], and $P2_1/m$ symmetry ($Z = 4$) at room temperature [22].

A closer look shows that the $C2/m$ and $C2/c$ descriptions are only subtly different. However, consideration of symmetry relationships shows that the $C2/m$ description is much more likely to be correct. Starting from the $LiCoO_2$ structure and removing the three-fold axis of the $R\text{-}3m$ space group results in a monoclinic unit cell with $C2/m$ symmetry, and a, c, and β

parameters that closely match the $C2/m$ descriptions of Li_2RuO_3 and Li_2PtO_3, and a b-axis that is 1/3 of the value reported for the Li_2MO_3 compositions. By replacing every third transition metal ion with Li^+ the b-axis is tripled leading directly to the $C2/m$ description of Li_2RuO_3 and Li_2PtO_3. The symmetry of the room temperature structure of Li_2RuO_3 is further lowered to $P2_1/m$ through the formation of Ru–Ru pairs. This is presumably an electronic distortion driven by metal–metal bonding interactions.

To confirm the structural details of the Li_2MO_3 phases, Rietveld refinements were carried out using the XRPD data. The Rietveld fits to the XRPD patterns are presented in Fig. 2. The results of the structural refinements for Li_2RuO_3 are in good agreement with the previously reported Li_2RuO_3 with $P2_1/m$ symmetry [22], while Li_2IrO_3 and Li_2PtO_3 are in good agreement with the isostructural Li_2MnO_3 possessing $C2/m$ symmetry [23].

The structural parameters obtained from the refinements of Li_2IrO_3 and Li_2PtO_3 are reported in Table 1. The accuracies of the refined structures are supported by the bond valence analyses presented in Table 2. The bond valence sums for the respective cations and anions are in good agreement with the expected oxidation states. This shows that even the light atom positions are determined with a reasonable degree of accuracy.

As seen in Fig. 2, we were not able to completely model the profiles of a number of peaks in the 2θ region between 19° and 33°. The asymmetry of these peaks originates from the presence of stacking faults associated with shifts between successive LiM_2 layers as previously observed for disordered Li_2MnO_3 [23] and Li_2PtO_3 [21], causing the classic Warren lineshape seen in Fig. 2 [24]. To partially account for the presence of stacking faults we have refined the cation site occupancies in the LiM_2 layers, within the constraint that the Li_2MO_3 stoichiometry is maintained. While this approach adequately accounts for changes in intensity of these peaks, it does nothing to improve the fit of the peak profiles.

Thus, it should be stressed that the disorder associated with the site occupancy values in Table 1 appears to be largely due to faults in stacking of highly ordered layers rather than random Li/M disorder. It should also be noted that concentration of stacking faults (as assessed by the peak broadening) looks to be smaller than most previous descriptions of these materials in the literature.

Table 1
Structural parameters for Li_2MO_3 ($M = $ Ir, Pt)—$C2/m$

Atom	Site	Occ	x	y	z	$B_{iso}/Å^2$
(a) Li_2IrO_3						
Ir(1)	4g	0.902(2)	0	0.3332(2)	0	0.39(4)
Li(1)	4g	0.098(2)	0	0.3332(2)	0	0.39(4)
Li(2)	2a	0.804(3)	0	0	0	0.39(4)
Ir(2)	2a	0.196(3)	0	0	0	0.39(4)
Li(3)	4h	1.0	0	0.809(6)	0.5	0.39(4)
Li(4)	2d	1.0	0	0.5	0.5	0.39(4)
O(1)	8j	1.0	0.252(4)	0.316(1)	0.759(2)	0.3
O(2)	4i	1.0	0.256(5)	0	0.788(3)	0.3

$a = 5.1633(2)$ Å, $b = 8.9294(3)$ Å, $c = 5.1219(2)$ Å, $\beta = 109.759(3)°$, $V = 222.2(2)$ Å^3, $R_{wp} = 19.800\%$, $R_{Bragg} = 5.382\%$, $\chi^2 = 2.283$

Atom	Site	Occ	x	y	z	$B_{iso}/Å^2$
(b) Li_2PtO_3						
Pt(1)	4g	0.917(1)	0	0.3331(2)	0	0.20(4)
Li(1)	4g	0.083(1)	0	0.3331(2)	0	0.20(4)
Li(2)	2a	0.834(3)	0	0	0	0.20(4)
Pt(2)	2a	0.166(3)	0	0	0	0.20(4)
Li(3)	4h	1.0	0	0.823(6)	0.5	0.20(4)
Li(4)	2d	1.0	0	0.5	0.5	0.20(4)
O(1)	8j	1.0	0.248(4)	0.319(1)	0.763(2)	0.3
O(2)	4i	1.0	0.260(5)	0	0.771(3)	0.3

$a = 5.1836(2)$ Å, $b = 8.9726(3)$ Å, $c = 5.1113(1)$ Å, $\beta = 109.864(2)°$, $V = 223.6(2)$ Å^3, $R_{wp} = 18.970\%$, $R_{Bragg} = 4.791\%$, $\chi^2 = 1.768$
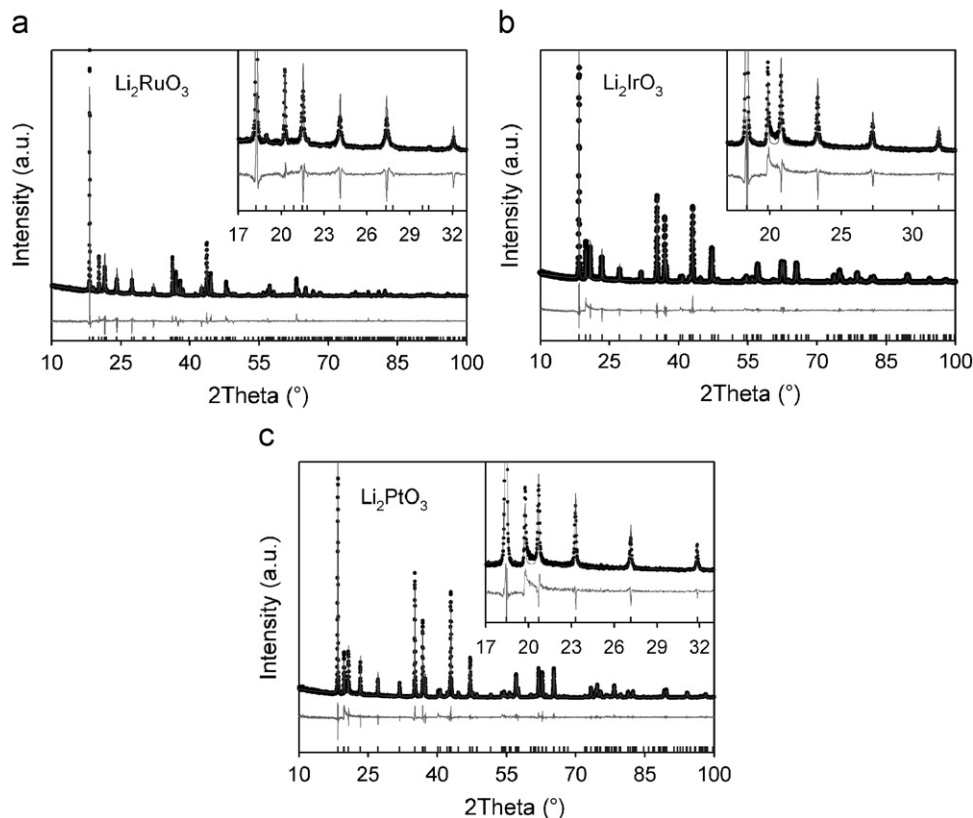B_{iso} fixed at 0.3 Å^2 for oxygen positions

Fig. 2. X-ray powder diffraction pattern and Rietveld refinement for (a) Li_2RuO_3 (b) Li_2IrO_3 (c) Li_2PtO_3: observed (●), calculated (line), and difference (bottom) profiles. Tick markers indicate the Bragg reflection positions.

Table 2
Bond lengths and bond valence values for Li_2IrO_3 and Li_2PtO_3

	Li_2IrO_3				Li_2PtO_3			
	Bond length (Å)		Bond valence		Bond length (Å)		Bond valence	
M–O	1.97(1)	×2	0.763(4)	×2	1.99(1)	×2	0.741(4)	×2
	2.01(1)	×2	0.685(3)	×2	2.04(1)	×2	0.647(3)	×2
	2.08(2)	×2	0.567(5)	×2	2.05(2)	×2	0.630(6)	×2
		BVS	4.036(8)			BVS	4.036(7)	
Li_2–O	1.97(3)	×2	0.335(5)	×2	2.06(3)	×2	0.201(3)	×2
	2.19(1)	×4	0.141(1)	×4	2.18(1)	×4	0.145(1)	×4
		BVS	1.236(5)			BVS	0.982(3)	
Li_3–O	1.88(3)	×2	0.327(5)	×2	1.97(4)	×2	0.249(5)	×2
	2.13(2)	×2	0.166(2)	×2	2.17(2)	×2	0.149(1)	×2
	2.35(4)	×2	0.092(2)	×2	2.23(4)	×2	0.127(2)	×2
		BVS	1.170(6)			BVS	1.050(6)	
Li_4–O	2.23(1)	×4	0.127(1)	×4	2.15(2)	×2	0.157(1)	×2
	2.24(2)	×2	0.123(1)	×2	2.22(1)	×4	0.130(1)	×4
		BVS	0.754(1)			BVS	0.888(2)	
O_1–M	1.97(1)	×1	0.763(4)	×1	1.99(1)	×1	0.741(4)	×1
	2.08(2)	×1	0.567(5)	×1	2.05(2)	×1	0.630(6)	×1
O_1–Li	1.88(3)	×1	0.327(5)	×1	1.98(4)	×1	0.249(5)	×1
	2.13(2)	×1	0.166(2)	×1	2.17(2)	×1	0.149(1)	×1
	2.19(1)	×1	0.141(1)	×1	2.18(1)	×1	0.145(1)	×1
	2.23(1)	×1	0.127(1)	×1	2.22(1)	×1	0.130(1)	×1
		BVS	2.091(9)			BVS	2.044(9)	
O_2–M	2.01(1)	×2	0.685(3)	×2	2.04(1)	×2	0.647(3)	×2
O_2–Li	1.97(3)	×1	0.336(5)	×1	2.06(3)	×1	0.201(3)	×1
	2.24(2)	×1	0.123(1)	×1	2.15(2)	×1	0.157(1)	×1
	2.35(4)	×2	0.092(2)	×2	2.23(4)	×2	0.137(2)	×2
		BVS	2.013(6)			BVS	1.926(5)	

Bond valence values for a given site were determined using the most abundant element, as such Li_1 from Table 1 is omitted.

Fig. 3. TGA for Li_2MO_3 (M = Ru, Ir, Pt) in O_2, air, N_2, and H_2:N_2 (5:95). The horizontal dashed lines represent the calculated weight percent for potential decomposition products.

As noted above attractive Ru–Ru interactions in Li_2RuO_3 are reported to lower the symmetry from $C2/m$ to $P2_1/m$. Because the two space groups have different systematic absences this distortion should give rise to additional reflections in the diffraction pattern. Such peaks can be observed at ~19.0° ($\bar{1}01$) and ~30.3° ($\bar{1}02$) as well as shoulders on more intense peaks near ~21.9° (100) and ~27.9° ($\bar{1}\bar{2}1$) in the XRPD patterns of Li_2RuO_3 (Fig. 2a). These peaks only appear for Li_2RuO_3 systems that show moderate to low degrees of faulting. No evidence of these extra peaks can be found in the XRPD patterns for Li_2IrO_3 and Li_2PtO_3 (Fig. 2b and c). Apparently increasing the d-orbital electron count from four (Ru^{4+}) to five (Ir^{4+}) or six (Pt^{4+}) destabilizes the electronic interactions responsible for this distortion.

3.1.1. Thermal stability

The thermal stabilities of Li_2RuO_3, Li_2IrO_3, and Li_2PtO_3, at elevated temperatures are of interest for high-temperature pH sensing applications. Thus, TGA was performed in O_2, air, N_2, and H_2:N_2 (5:95), the resulting plots are presented in Fig. 3. The compounds have similar stabilities in O_2, air and N_2. Under these non-reducing atmospheres they are stable, as determined by the onset of weight loss, up to ~1525, ~1475, and ~1375 K for Li_2RuO_3, Li_2IrO_3, and Li_2PtO_3, respectively. The increasing thermal stability upon going from Pt to Ir to Ru correlates with the decrease in noble character of the metallic element. We also note a small weight loss beginning at ~475 K of 0.49%, 0.60%, and 0.18% for Li_2RuO_3, Li_2IrO_3, and Li_2PtO_3, respectively. The origin of this feature is not certain, but it may be caused by the loss of water.

All three phases show reduced thermal stability in forming gas, H_2:N_2 (5:95). Li_2PtO_3 and Li_2RuO_3 lose weight in two steps. The
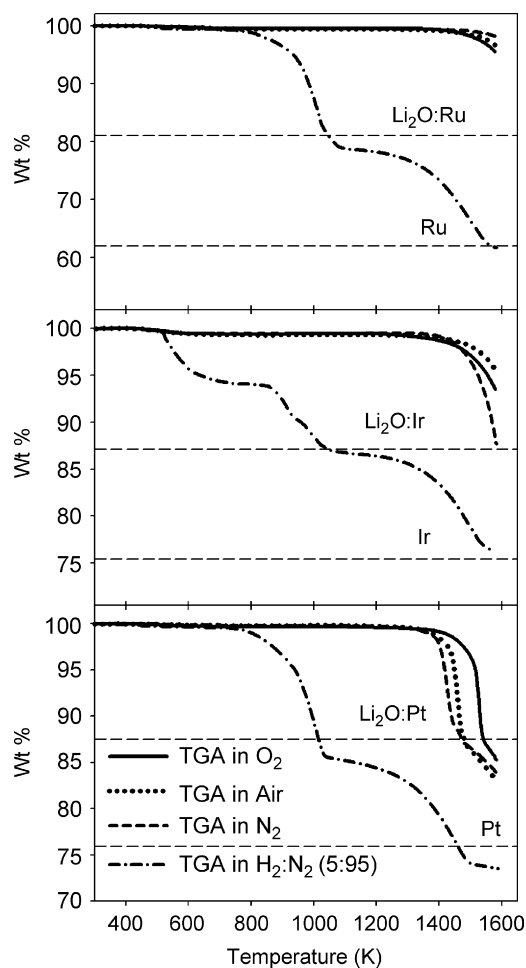
first weight loss takes place over the approximate temperature range 800–1000 K. *Ex-situ* XRPD measurements of quenched samples show that this step corresponds to reduction of the platinum group metal to its elemental state accompanied by exsolution of lithium oxide. The upper set of dashed lines in Fig. 3 show the theoretical weight loss corresponding to the decomposition reaction: $Li_2MO_3(s) \rightarrow Li_2O(s) + M(s) + O_2(g)$. The differences between the calculated and observed mass losses likely result from a fractional amount of Li_2O decomposition and/or volatilization prior to reaching the observed plateau. Further heating leads to complete loss of Li_2O (see lower set of dashed lines), as seen in Fig. 3.

The TGA of Li_2IrO_3 in forming gas differs from those of Li_2PtO_3 and Li_2RuO_3. An additional weight loss begins around 475 K, reaching a plateau at ~94 wt%. This feature suggests formation of an intermediate phase along the decomposition pathway. To better understand this behavior *in-situ* XRPD experiments were performed. Not withstanding the inevitable temperature and heating rate differences between the two measurements a cursory look at the *in-situ* XRPD data (Fig. 4) indicates that Li_2IrO_3 decomposes into Ir and a Li_2O-like phase. The XRPD patterns above 550 °C are dominated by the diffraction peaks of metallic iridium. In addition there are a couple of weak peaks that cannot be unambiguously identified. Nevertheless, on cooling the peak at 32.1° shifts to ~33.6°, which is exactly where the strongest peak for Li_2O, the (111) peak, is expected. Thus we conclude that the weak peaks seen in Fig. 4 originate from Li-containing phases.
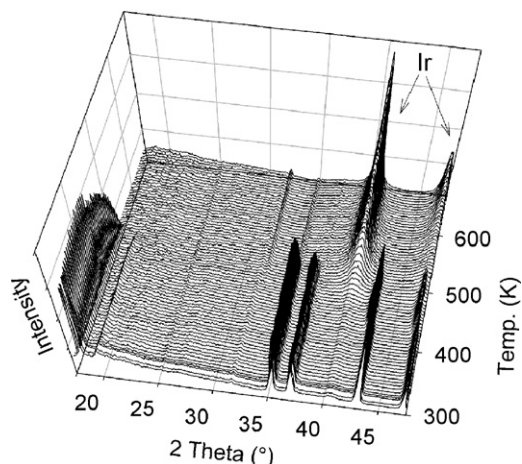
Fig. 4. *In-situ* X-ray powder diffraction patterns of Li_2IrO_3 in forming gas (H_2:N_2, 5:95) from 300 to 675 K with 5 K increments.
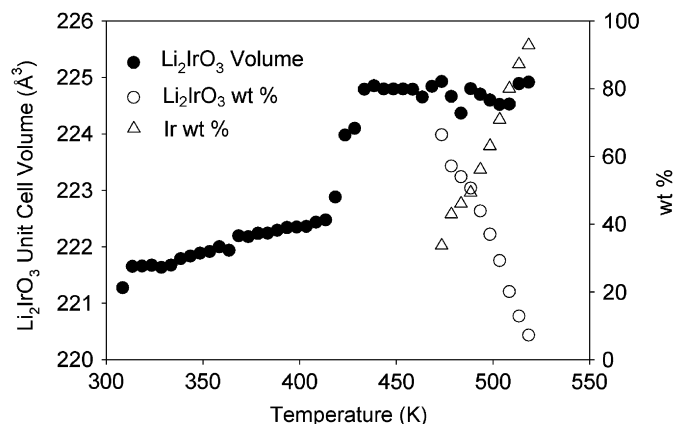

Fig. 5. Unit cell volume evolution of Li_2IrO_3 and the refined phase fractions of Ir and Li_2O during reduction in forming gas (H_2:N_2, 5:95) as obtained from the Rietveld refinements.

Upon closer inspection, shifts in the positions of several diffraction peaks for Li_2IrO_3 are observed. Fig. 5 shows the unit cell volume of the Li_2IrO_3 phase as determined from the *in-situ* XRPD data. There is an abrupt increase of ∼1% in the unit cell volume that precedes the decomposition. Loss of oxygen and the corresponding reduction of Ir^{4+} would be expected to both increase the unit cell volume and trigger a weight loss. However, a 6% weight loss corresponds to loss of one oxygen ion per formula unit and it is difficult to imagine how Li_2IrO_3 could accommodate such a degree of oxygen loss while maintaining its structural integrity. Further study is needed to fully understand the thermal decomposition of Li_2IrO_3, but it does not appear as though a structurally distinct intermediate phase exists.

3.1.2. Electronic structure calculations

To better understand the properties of the Li_2MO_3 phases electronic band structure calculations were performed on the structures obtained for Li_2IrO_3 and Li_2PtO_3. The electronic structure of Li_2RuO_3 is complicated by the symmetry lowering distortion of the Ru-sublattice. A full computational study of this distortion is in progress and will be published elsewhere.

Electronic DOS plots for Li_2IrO_3 and Li_2PtO_3 are presented in Fig. 6. The octahedral coordination of Ir^{4+} and Pt^{4+} splits the d-orbitals into t_{2g} (π^*) and e_g (σ^*) states. The 2D edge-sharing connectivity of the MO_6 octahedra in Li_2MO_3 broadens the antibonding M–O levels into bands. The t_{2g} (π^*) states are 5/6 and completely filled in Li_2IrO_3 and Li_2PtO_3, respectively. The Fermi level cuts through the t_{2g} (π^*) band in Li_2IrO_3, suggesting metallic character. The electronic structure of Li_2PtO_3 is clearly that of a semiconductor with a gap of 2.32 eV between the filled t_{2g} (π^*) and empty e_g (σ^*) bands. These results agree with expectations based on a simple consideration of the d-orbital filling.

Upon moving from Ir to Pt there is a decrease in the energy separation of the bands that are nominally labeled as O $2p$ bands[1] and the t_{2g} (π^*) states. This is a reflection of the increasingly covalent character of the M–O bonds. While these two sets of bands are separated in Li_2IrO_3, the gap has completely collapsed for Li_2PtO_3. Another measure of the bond covalency is seen in the fact that the O $2p$ orbitals and the Pt $5d$ orbitals contribute almost equally to both the bonding states (-5 to -7 eV) and antibonding states (>-2 eV). Thus the Pt–O bonding in Li_2PtO_3 is almost fully
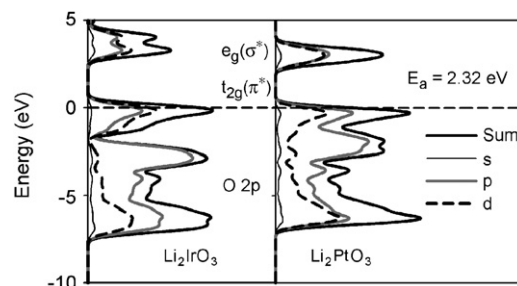
Fig. 6. The electronic density of states (DOS) plots for Li_2MO_3 (M = Ir, Pt). The d-orbital contribution can be completely attributed to the platinum group metal, while the p-orbital contribution comes predominantly from oxygen. The horizontal dashed line depicts the Fermi energy.

covalent. The increased covalency correlates well with the thermal stability observed in oxidizing and inert atmospheres.

3.1.3. Optical properties

The UV–visible diffuse reflectance spectra for Li_2IrO_3 and Li_2PtO_3 are presented in Fig. 7. The Li_2IrO_3 is strongly absorbing in the visible spectrum and hence black in appearance. Li_2PtO_3 is bright yellow and only begins to strongly absorb at wavelengths <500 nm. By extrapolating the absorbance in the UV–visible spectrum to zero absorbance a band gap of 2.3 eV for Li_2PtO_3 is obtained. This value is in excellent agreement with the calculated band gap of 2.32 eV.

3.1.4. Electrical measurements

The electrochemical impedance spectroscopy measurements for Li_2PtO_3 are shown in Fig. 8. Because the measurements were made on a polycrystalline pellet of limited density, 63.1% theoretical, our interpretation is limited to qualitative features.

The impedance of the Li_2PtO_3 sample decreases rapidly with increasing temperature, indicating activated carrier transport. The conductivities determined upon extrapolation to a frequency of 0 Hz were used to construct an Arrhenius plot (Fig. 9), from which an activation energy of, 0.92(5) eV was extracted. The difference between this value and the optical band gap (2.3 eV) is not immediately obvious. It is worth noting, the activation energy reported here is almost twice the value of 0.49 eV previously reported for Li_2PtO_3 [20]. The origin of this discrepancy is not clear, but X-ray patterns suggest that the earlier studies were carried out on a sample with a higher degree of stacking faults.
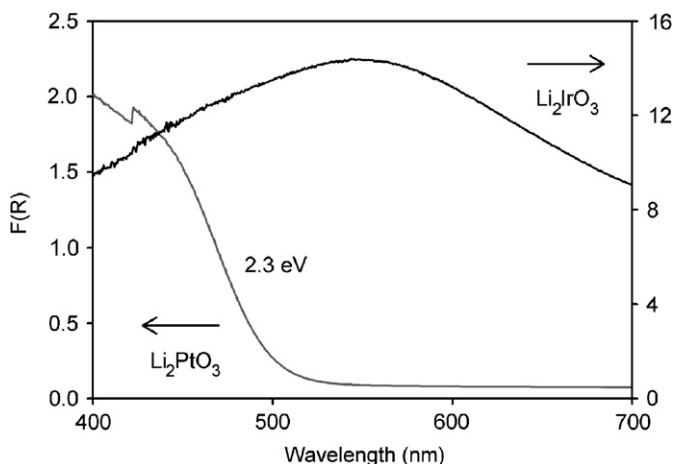
---

[1] The lower energy "O $2p$" bands are actually M d–O $2p$ bonding gradually giving way to nonbonding O $2p$ bands as the energy increases.

Fig. 7. Plot of UV–vis diffuse reflectance spectra converted to absorbance using the Kubelka–Munk function for Li_2IrO_3 and Li_2PtO_3.
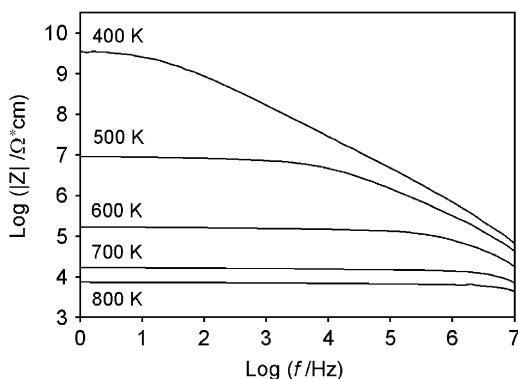

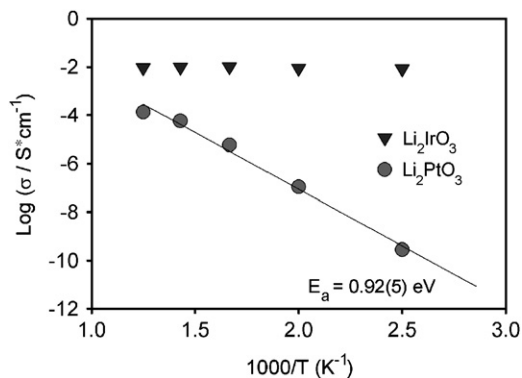**Fig. 8.** Impedance spectra from 1 to 10^7 Hz for Li_2PtO_3 from 400 to 800 K.

Fig. 9. Conductivity plot, $\log(\sigma) = f(10^3/T)$, of Li_2MO_3 (M = Ir, Pt) with corresponding linear fit (line) for the semiconducting Li_2PtO_3 used to determine the reported activation energies.

It appears that the conductivities of these systems are dependent on the method of preparation and the degree of stacking fault disorder present.

Fig. 9 also presents the temperature dependence of Li_2IrO_3 conductivities determined upon extrapolation to a frequency of 0 Hz. Although the measured conductivities for these two compounds are not as high as might be expected for a metallic conductor, Li_2IrO_3 shows little temperature dependence. This behavior, taken together with the electronic structure calculations

suggest this phase is in fact a metallic conductor. The relatively low absolute conductivity observed for Li_2IrO_3 is likely a result of the combined effects of incomplete sintering of the pellets and the anisotropic nature of the electronic structure.

Given the structural similarities to well-known Li^+-ion conductors, such as $LiCoO_2$, we considered the possibility that Li^+ conduction may be contributing to the total conductivity, of the semiconducting Li_2PtO_3. If the ionic conductivity was a significant portion of the total conductivity the resistance should increase as one proceeds to higher frequencies due to the inability of the ions to respond to high frequency changes in field, but this is not observed. Therefore, it is reasonable to assume that electronic conductivity dominates any contribution from ionic conductivity to the total conductivity.

4. Conclusions

The Li_2MO_3 (M = Ru, Ir, Pt) systems are thermally stable against reduction in air, O_2, and N_2 below 1375 K, which is an attractive feature for sensor operation over a wide range of temperatures. The thermal stability is significantly reduced in forming gas (N_2:H_2), where Li_2RuO_3 and Li_2PtO_3 are stable up to ~850 K, while Li_2IrO_3 is stable to ~450 K. Thermal analysis coupled with *ex-situ* and *in-situ* diffraction measurements show that Li_2MO_3 compounds decompose through reduction of the platinum group metal cation to its elemental state combined with exsolution of Li_2O. Li_2IrO_3 undergoes a slightly more complicated decomposition, which appears to involve loss of oxygen prior to collapse of the layered Li_2IrO_3 structure.

Optical measurements, electronic structure calculations, and impedance measurements indicate that Li_2IrO_3 is a metallic conductor, while Li_2PtO_3 is a semiconductor. Relatively high electronic conductivity is a prerequisite for a material to effectively function as a pH sensing material. Thus Li_2PtO_3 is unlikely to behave favorably for this application. In contrast, the formation of metallic Li_2IrO_3 is observed when iridium metal is reacted with either a stoichiometric amount or even a large excess of Li_2CO_3. This may help to explain why pH sensors made from lithium carbonate melt oxidation of Ir wires are superior to sensors produced from a similar treatment of platinum.

References

[1] A. Fog, R.P. Buck, Sensors Actuators 5 (1984) 137.
[2] K.G. Kreider, M.J. Tarlov, J.P. Cline, Sensors Actuators B 28 (1995) 167.
[3] M. Wang, S. Yao, Electroanalysis 15 (2003) 1606.
[4] S. Yao, M. Wang, J. Electrochem. Soc. 149 (2002) H28.
[5] S. Yao, M. Wang, M. Madou, J. Electrochem. Soc. 148 (2001) H29.
[6] J.F. Dulac, C.R. Acad. Sci. Paris Ser. B 270 (1970) 223.
[7] A.C.W.P. James, J.B. Goodenough, J. Solid State Chem. 74 (1988) 287.
[8] H. Kobayashi, R. Kanno, Y. Kawamoto, M. Tabuchi, O. Nakamura, M. Tanako, Solid State Ionics 82 (1995) 25.
[9] H. Kobayashi, M. Tabuchi, M. Shikano, H. Kageyama, R. Kanno, J. Mater. Chem. 13 (2003) 957.
[10] K. Asakura, S. Okada, H. Arai, S.-I. Tobishima, Y. Sakurai, J. Power Sources 81–82 (1999) 388.
[11] A. Alexander, P.D. Battle, J.C. Burley, D.J. Gallon, C.P. Grey, S.H. Kim, J. Mater. Chem. 13 (2003) 2612.
[12] P. Kroeschell, R. Wolf, R. Hoppe, Z. Anorg. Allg. Chem. 536 (1986) 81.
[13] K. Schwartz, J. Parise, C. Prewitt, R. Shannon, Acta Crystallogr. B 38 (1982) 2109.
[14] H.M. Rietveld, J. Appl. Crystallogr. 2 (1969) 65.
[15] A.A. Coelho, Topas Academic 2004.
[16] I.P. Shapiro, Opt. Spektrosk. 4 (1958) 256.

[17] W. Milman, B. Winkler, J.A. White, C.J. Pickard, M.C. Payne, E.V. Akhmatskaya, R.H. Nobes, Int. J. Quant. Chem. 77 (2000) 77895.

[18] J.P. Perdew, J.A. Chevary, S.H. Vosko, K.A. Jackson, M.R. Pederson, D.J. Singh, C. Fiolhais, Phys. Rev. B 46 (1992) 6671.

[19] J.P. Perdew, Y. Wang, Phys. Rev. B 40 (1986) 8600.

[20] S. Okada, J.-I. Yamaki, K. Asakura, H. Ohtsuka, H. Arai, S.-I. Tobishima, Y. Sakurai, Electrochim. Acta 45 (1999) 329.

[21] M. Casas-Cabanas, J. Rodriguez-Carvajal, J. Canales-Vazquez, Y. Laligant, P. Lacorre, M.R. Palacin, J. Power Sources 174 (2007) 414.

[22] Y. Miura, Y. Yasui, M. Sato, N. Igawa, K. Kakurai, J. Phys. Soc. Japan 76 (2007) 033705.

[23] J. Bréger, M. Jiand, N. Deupré, Y.S. Meng, Y. Shao-Horn, G. Ceder, C.P. Grey, J. Solid State Chem. 178 (2005) 2575.

[24] B.E. Warren, Phys. Rev. 59 (1941) 693.